Chemical Science

ROYAL SOCIETY OF CHEMISTRY

EDGE ARTICLE

View Article Online
View Journal | View Issue

Cite this: *Chem. Sci.*, 2023, **14**, 1234

All publication charges for this article have been paid for by the Royal Society of Chemistry

Single-atom engineering of hemicyanine and its amphiphilic derivative for optimized near infrared phototheranostics†

Shankun Yao,[ac] Yuncong Chen, *[acd] Weizhong Ding,[a] Fengwu Xu,[a] Zhipeng Liu,[b] Yaheng Li,[a] Yanping Wu,[a] Shumeng Li,[a] Weijiang He [ac] and Zijian Guo *[acd]

Received 30th October 2022
Accepted 19th December 2022

DOI: 10.1039/d2sc05982g

rsc.li/chemical-science

Near-infrared (NIR) dyes are widely used in the field of *in vivo* phototheranostics. Hemicyanine dyes (HDs) have recently received tremendous attention due to their easy synthesis and excellent NIR features. However, HDs can easily form non-fluorescent aggregates and their potential for phototherapy still needs further exploration due to their poor ability to generate reactive oxygen species (ROS). Herein, a series of hemicyanine dyes with different chalcogen atom (O, S, Se) substitutions were constructed to achieve optimized potential for phototheranostics. By replacing O with the heavy atom Se in the xanthene skeleton, CySe-NEt_2 showed much more favourable features such as extended NIR absorption/emission wavelength, boosted $^1O_2$ generation rate and higher photothermal effect. In addition, a poly(ethylene glycol) (PEG) group was introduced into the scaffold and yielded a nanotheranostic agent CySe-$mPEG_{5K}$, which easily formed nanoparticles with appealing features such as excellent photostability, effective prevention of unpleasant H-aggregation, fast/selective tumor accumulation and minimum dark toxicity. Solid tumor growth was significantly suppressed through combined photodynamic therapy (PDT) and photothermal therapy (PTT) guided by NIR fluorescence (NIRF) and photoacoustic (PA) imaging. This study not only presents the first example of selenium-substituted hemicyanine dyes, but also offers a reliable design strategy for the development of potent NIR phototheranostic agents with multi-mode imaging-guided combination therapeutic ability.

Introduction

Phototheranostics, composed of deep tissue optical imaging diagnosis and phototherapy, has shown great potential in overcoming inherent complex challenges in cancer treatment.[1–3] NIR dyes with deeper imaging and therapeutic depth are more appealing for better phototheranostic performance. Photodynamic therapy (PDT) and photothermal therapy (PTT) have received tremendous attention owing to their excellent spatial specificity, noninvasiveness, and minimal side effect to normal tissues over traditional chemotherapy and radiotherapy.[4–6] PDT is an efficient tumor therapy that combines photosensitizers (PSs) and excitation light at a specific wavelength to produce reactive oxygen species (ROS), especially singlet oxygen ($^1O_2$) to damage or destroy surrounding cells.[7–10] PTT takes advantage of photothermic agents which could convert light into heat to elevate the local environment temperature and subsequently kill cancerous cells. However, the effectiveness of a single phototherapy modality is unsatisfactory, often limited by the hypoxic microenvironment, penetration depth or the power of light excitation.[11] From the perspective of synergistic therapy, the combination of PDT and PTT is considered as a practical approach to achieve superimposed effects while overcoming their respective deficiencies.[12–15] Moreover, the photoinduced thermal effect could generate ultrasonic waves by local tissue thermoelastic expansion, which could be utilized for photoacoustic imaging (PAI) with deeper tissue imaging penetration and a high spatial resolution image of ~100 mm when compared with the NIR fluorescence imaging technique.[16–18]

Hemicyanine dyes (HDs) are extensively used as near-infrared fluorescence (NIRF) reporters for targeted anticancer drug delivery monitoring and imaging applications of various biological species such as reactive oxygen species (ROS), reactive nitrogen species (RNS), biothiols, metal ions and enzymes, as well as intracellular pH changes.[19–24] Researchers

[a]*State Key Laboratory of Coordination Chemistry, Coordination Chemistry Institute, School of Chemistry and Chemical Engineering, Nanjing University, Nanjing 210023, P. R. China. E-mail: chenyc@nju.edu.cn; zguo@nju.edu.cn*

[b]*College of Materials Science and Engineering, Nanjing Forestry University, Nanjing, 210037, P. R. China*

[c]*Chemistry and Biomedicine Innovation Center (ChemBIC), Nanjing University, Nanjing 210023, P. R. China*

[d]*Nanchuang (Jiangsu) Institute of Chemistry and Health, Nanjing 210000, Jiangsu, P. R. China*

† Electronic supplementary information (ESI) available. See DOI: https://doi.org/10.1039/d2sc05982g

have made remarkable progress in developing hemicyanine-based activatable probes through the output of fluorescence/PA signals for *in vivo* imaging and early diagnosis of diseases including inflammation, acute organ failure, Alzheimer's disease, depression, diabetes and cancer.[25–27] However, their application as efficient phototheranostic reagents is far from satisfactory and needs further exploration. To date, a commonly employed approach to enhance photosensitivity is to incorporate heavy atoms into the hemicyanine chromophores to improve their intersystem crossing (ISC) efficiency and ROS generation.[28–30] For example, Peng's group reported a hypoxia-activated iodine substituted hemicyanine dye ICy-N for precise tumor hypoxia imaging and restrained tumor growth through the PDT process.[31] However, the introduction of heavy atoms (Br, I) failed to substantially extend the absorption/emission wavelength of HDs. Recent studies showed that replacing an oxygen atom in a hemicyanine derivative with a sulfur atom could enhance photothermal efficiency and achieve efficient PTT in a tumor-bearing mouse model, but showed very limited improvement in $^1O_2$ efficiency for PDT.[32,33] On the other hand, due to the strong π–π and electrostatic interactions, hemicyanine derivatives tend to form H-aggregates and quench both fluorescence intensity and singlet oxygen quantum yield (Φ_Δ) dramatically in aqueous solution, which significantly limit their theranostic performance. Therefore, there are still great challenges in expanding the imaging window of hemicyanine dyes and improving their therapeutic efficacy while avoiding photobleaching and dark toxicity.

Herein, a series of NIR hemicyanine derivatives (CyX-NEt$_2$, X = O, S, Se) were designed and synthesized through single-atom engineering in the xanthene ring (Scheme 1). Compared to CyO-NEt$_2$ and CyS-NEt$_2$, the Se-substituted hemicyanine CySe-NEt$_2$ showed distinct advantages such as longer absorption/emission wavelengths (776/818 nm), significantly enhanced $^1O_2$ generation rate (14.8%) and elevated photothermal conversion efficiency (PCE, 42.2%). The improved theranostic potential of CySe-NEt$_2$ could be attributed to increased ISC efficiency and better utilization of triplet states, which was supported by theoretical calculations. Although CySe-NEt$_2$ exhibited the best phototherapeutic effect among the three compounds, it showed poor photostability and increased dark toxicity. A nanotheranostic photosensitizer CySe-mPEG$_{5K}$ was synthesized by introducing a poly(ethylene glycol) (PEG) chain. This modification not only improved the photostability and biocompatibility, but also showed advantages including suppression of the unfavoured H-aggregation and fast/selective tumor accumulation. CySe-mPEG$_{5K}$ showed excellent performance on multimodal imaging-guided combinational PDT–PTT against tumors with negligible side effects *in vivo*.

Results and discussion

Design and synthesis of the O-, S-, and Se-substituted hemicyanine derivatives

HDs were chosen as the molecular platform for NIRF/PA dual imaging because they possess a large molar extinction coefficient (>10^5 M^{-1} cm^{-1}) and highly diverse structural tunability in the NIR region. Although the most commonly used HDs possess high fluorescence quantum yield, they usually show low Φ_Δ and unsatisfactory photothermal effect, which limit their application in phototheranostics. We envisioned that Se-substitution in the xanthene ring could help improve the ISC efficiency due to the heavy-atom effect of Se, which could lead to less decay *via* the singlet state. Due to the long triplet lifetime, a higher possibility of nonradiative decay to generate heat for PTT and related PA signal for PAI, as well as higher $^1O_2$ generation rate for better PDT, are expected. CyO-NEt$_2$ and CyS-NEt$_2$ were prepared according to the reported procedures and

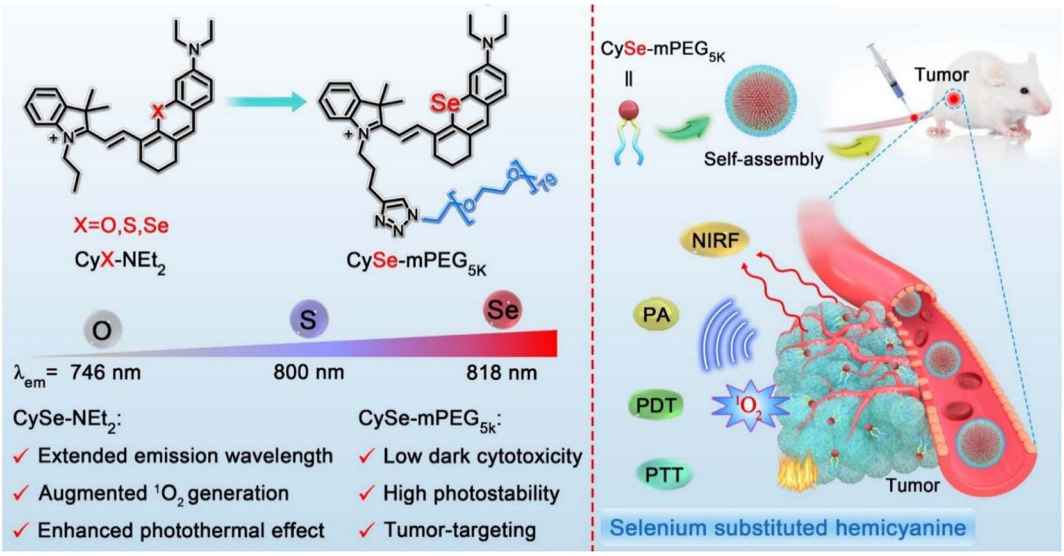

Scheme 1 Chemical structures of CyX-NEt$_2$ (X = O, S, Se) and CySe-mPEG$_{5K}$, and the schematic illustration of tumor targeting imaging-guided phototherapy.

used as control compounds. CySe-NEt_2 was obtained from the dye IR780 and 3-diethylamino-phenylselenol in an alkaline medium as shown in Scheme S1.† Given the importance of photostability and the tumor targeting ability of PSs in tumor ablation, a macrotheranostic agent CySe-$mPEG_{5K}$ composed of the NIR dye CySe-NEt_2 linked with a long PEG chain was also designed and synthesized through a copper(I)-catalyzed alkyne–azide cycloaddition (CAAC) reaction. All the CyX-NEt_2 compounds have been fully characterized by ^{1}H NMR and ^{13}C NMR and high-resolution mass spectrometry (HRMS), while CySe-$mPEG_{5K}$ was characterized by ^{1}H NMR, High Performance Liquid Chromatography (HPLC) and Modi-TOF, as shown in Fig. S19–S37†.

Spectroscopic and photosensitivity studies of CyX-NEt_2 (X = O, S, Se) *in vitro*

The absorption and emission spectra of CySe-NEt_2 (λ_{abs} = 776 nm, λ_{em} = 818 nm) showed a distinct redshift compared to CyO-NEt_2 (λ_{abs} = 716 nm, λ_{em} = 746 nm) and CyS-NEt_2 (λ_{abs} = 760 nm, λ_{em} = 800 nm) in methanol as well as in other solvents (Fig. 1a–c and S1,† Table 1). The longer absorption/emission wavelengths of CySe-NEt_2 endowed it with the potential for better tissue penetration than CyO-NEt_2 and CyS-NEt_2. CySe-NEt_2 retained the feature of high molar absorptivity (>10^5 M^{-1} cm^{-1}) of hemicyanine dyes. The fluorescence quantum yield of CySe-NEt_2 (Φ_f = 0.11) was lower than those of

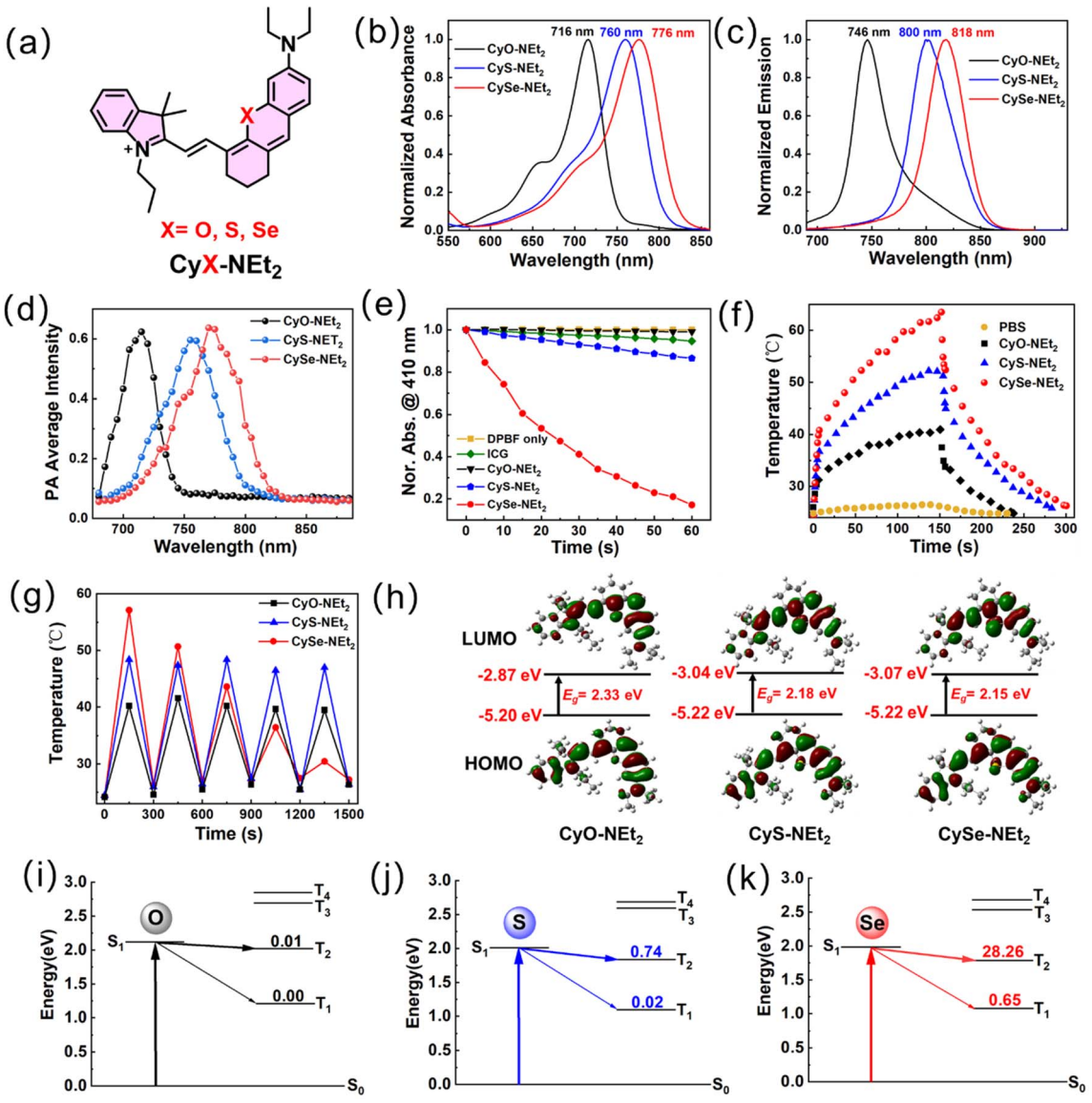

Fig. 1 (a) Chemical structures of CyX-NEt_2 (X = O, S or Se). Normalized (b) absorption and (c) emission (λ_{ex}, 670 nm) spectra of CyX-NEt_2 in methanol solvent. (d) Photoacoustic spectra of CyX-NEt_2 (X = O, S, Se). (e) Absorbance at 415 nm for DPBF degradation with different compounds under 750 nm light irradiation (5 mW cm^{-2}). (f) Photothermal effects for heat transfer of CyX-NEt_2 in PBS (750 nm laser, 500 mW cm^{-2}). (g) Photothermal stability study of CyX-NEt_2 in PBS during five circles of heating–cooling processes. (h) HOMO–LUMO electron cloud distribution and energy levels of CyX-NEt_2. (i–k) Possible ISC channels and the corresponding values of $[\langle S_n|H_{SO}|T_m\rangle/\Delta E_{S_nT_m}]^2$ for (i) CyO-NEt_2, (j) CyS-NEt_2 and (k) CySe-NEt_2.

Table 1 Photophysical and photosensitizing properties of CyX-NEt_2 compounds

Compound	λ_{abs}[a] (nm)	ε[a] (10^5 M^{-1} cm^{-1})	λ_{em}[a] (nm)	Φ_f[a,b]	S_1[c] (eV)	R[d] ($\times 10^6$)	Φ_Δ[e]	PCE[f]
CyO-NEt_2	716	1.37	746	0.23	2.14	0.01	0.9%	27.5%
CyS-NEt_2	760	1.17	800	0.18	2.00	0.76	2.5%	38.5%
CySe-NEt_2	776	1.08	818	0.11	1.97	28.91	14.8%	42.2%

[a] In methanol. [b] Fluorescence quantum yield estimated with ICG as the standard. [c] S_1 is the calculated energy of the first singlet excited state. [d] $R = [\langle S_n|H_{SO}|T_m\rangle/\Delta E_{S_nT_m}]^2$. [e] Singlet oxygen quantum yield was determined with respect to ICG. [f] In PBS buffer.

CyO-NEt_2 (Φ_f = 0.18) and CyS-NEt_2 (Φ_f = 0.23), which was reasonable due to the Se-accelerated ISC and the faster internal conversion at the longer wavelength. From CySe-NEt_2 to CyO-NEt_2, although there was a 52% loss in the fluorescence quantum yield, the much longer excitation/emission wavelength of CySe-NEt_2 will lead to a better imaging depth. In addition, a distinct redshift of the PA signal was observed for CySe-NEt_2 compared to its O- and S-substituted counterparts, which was in good accordance with the absorption spectra (Fig. 1d and S2†).

To evaluate the potential of this new scaffold for phototherapy, we continued to conduct a series of validation experiments including $^1O_2$ production capacity and the photothermal conversion efficacy. The $^1O_2$ generation was firstly detected in methanol under 750 nm laser (5 mW cm^{-2}) irradiation using DPBF as the indicator. It could be seen that DPBF could hardly be degraded by CyO-NEt_2 and showed a slight change of absorption signal in the presence of CyS-NEt_2, indicating the limited photosensitive ability (Fig. S3a and b†). Interestingly, the irradiation of CySe-NEt_2 caused a dramatic decrease in the absorption signal of DBPF at 410 nm, which clearly suggests photosensitized $^1O_2$ generation. A different singlet oxygen capture agent SOSG was used to demonstrate the superior $^1O_2$ generation ability of CySe-NEt_2 in methanol and PBS buffer (Fig. S4†). Using ICG as a reference, the Φ_Δ of CyO-NEt_2, CyS-NEt_2 and CySe-NEt_2 were calculated to be 0.9%, 2.5% and 14.8%, respectively (Fig. 1e and S3d–i†). As expected, the photothermal conversion efficiency (PCE) of CySe-NEt_2 (42.2%) was higher than those of CyO-NEt_2 (27.5%) and CyS-NEt_2 (38.5%) (Fig. 1f and S5,† Table 1). When oxygen atom was replaced by selenium atom, an over 15-fold increase of the $^1O_2$ generation ability and a 53% enhancement of PCE were achieved, suggesting a more efficient utilization of excited states for phototherapy. However, the curves of thermal-cooling ON/OFF cycles showed that the photostability of CySe-NEt_2 was poor compared to those of CyO-NEt_2 and CyS-NEt_2, which may be ascribed to the $^1O_2$-mediated cleavage of polyenes and thermal-induced decomposition (Fig. 1g).[34] These results suggested that CySe-NEt_2 could act as a superior phototheranostic agent compared to CyO-NEt_2 and CyS-NEt_2, but it still needs to face the challenge of photostability.

The density functional theory (DFT) calculation was conducted to investigate the mechanism of action of CySe-NEt_2 as a better phototheranostic agent (Fig. 1h–k, Tables 1, S2 and S3†). The HOMO–LUMO energy gaps of CyO-NEt_2, CyS-NEt_2, and CySe-NEt_2 were calculated to be 2.33, 2.18 and 2.15 eV, respectively (Fig. 1g). The narrower band gap of CySe-NEt_2 could be ascribed to the increased atomic radius and change in electronegativity. The spin–orbit coupling (SOC) constants significantly increased, and the singlet–triplet energy gap (ΔE_{ST}) decreased upon replacing oxygen and sulfur with the heavy atom selenium, resulting in a tremendous enhancement in the ISC rate constant k_{ISC} ($\propto[\langle S_n|H_{SO}|T_m\rangle/\Delta E_{S_nT_m}]^2$) for CySe-$NEt_2$. The ISCs from the S_1 states to the T_2 states were found to be the dominant contributor to the formation of the triplet states. The k_{ISC} of CySe-NEt_2 was estimated to be ~38 times and >2800 times larger than those of CyS-NEt_2 and CyO-NEt_2, respectively (Fig. 1h–k and Table 1). The DFT calculations strongly supported the experimental findings that the introduction of Se atom endowed CySe-NEt_2 with excellent potential as a theranostic agent.

Cytotoxicity assessment of CySe-NEt_2

The cellular uptake and subcellular localization of the compound CyX-NEt_2 (X = O, S, Se) were assessed by confocal laser scanning microscopy (CLSM). As illustrated in Fig. S6,† the fluorescence intensity of CyX-NEt_2 in 4T1 cells significantly increased over the incubation time and reached saturation at about 30 min. Then, the colocalization experiments of CyX-NEt_2 were investigated using commercial fluorescent organelle-selective trackers (Mito-Tracker Green, Lyso-Tracker Green and Hoechst 33342). As shown in Fig. S7,† the fluorescence signals of the CyX-NEt_2 stained cells well overlapped those of Mito-Tracker Green incubated cells with Pearson's correlation coefficients (PCCs) of 0.89, 0.89 and 0.91 for CyO-NEt_2, CyS-NEt_2 and CySe-NEt_2 respectively. This result was reasonable due to the lipophilic cationic features of CyX-NEt_2.[35] Next, the intracellular ROS generated by CyX-NEt_2 were evaluated in 4T1 cells using a cell-permeable ROS probe 2′,7′-dichlorofluorescein diacetate (DCFH-DA). In Fig. 2a and b, the 4T1 cells incubated with CyX-NEt_2 in the dark were almost nonemissive. After irradiation for 10 min, the fluorescence intensity in CySe-NEt_2 incubated cells increased dramatically and was much stronger than those in CyO-NEt_2 and CyS-NEt_2 incubated cells, demonstrating that the intracellular ROS generation ability of CySe-NEt_2 was much better than those of CyO-NEt_2 and CyS-NEt_2. As ROS generation by mitochondria-targeted PSs could readily cause mitochondrial membrane potential (MMP) loss, MMP changes were assessed by JC-1 staining. 4T1 cells treated with CySe-NEt_2 demonstrated an obvious MMP reduction in comparison with light-only treatment (Fig. S8†). These results indicated that CySe-NEt_2 is a potent photosensitizer with

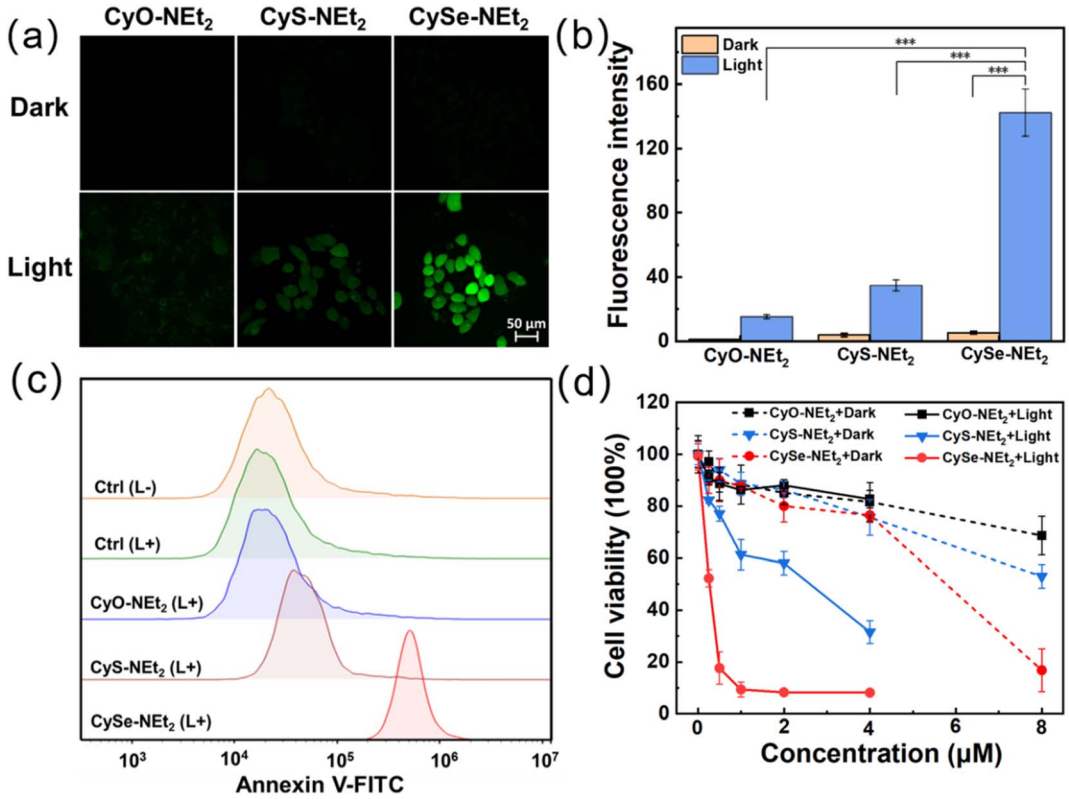

Fig. 2 (a) Intracellular ROS production in 4T1 cells incubated with DCFH-DA and CyX-NEt_2 (X = O, S or Se) in the dark and under 750 nm light irradiation. (b) Average fluorescence emission intensities of 4T1 cell in (a). (c) Flow cytometry analysis of 4T1 cells stained with annexin V-FITC after different treatments. Dose = 2.0 μM. (d) Cell viability of 4T1 cells treated with CyX-NEt_2 at various doses in the dark and under 750 nm light irradiation (6.0 J cm^{-2}). Data are expressed as mean ± SD. *P < 0.05, **P < 0.01, ***P < 0.001.

mitochondria-targeting ability and could initiate intracellular ROS overproduction and distinct MMP loss.

Furthermore, flow cytometry analysis was performed to unveil the cell death mechanism using an annexin-V/FITC-PI kit. As shown in Fig. 2c and S9,† after incubation with CySe-NEt_2 and 750 nm light irradiation (2 μM, 6.0 J cm^{-2}, 5 min), more than 90% of the 4T1 cells were in the apoptosis stage. By contrast, CyO-NEt_2 treatment did not cause significant cell death population and 22% of CyS-NEt_2 treated 4T1 cells experienced apoptotic cell death. Next, we studied the anticancer effect of CyX-NEt_2 on 4T1 cells by the methyl thiazolyl tetrazolium (MTT) assay to further confirm the application of CySe-NEt_2 as a potential phototherapeutic agent. As shown in Fig. 2d, under a low dose of 750 nm laser irradiation (6.0 J cm^{-2}), CySe-NEt_2 significantly inhibited cell proliferation with a half maximal inhibitory concentration (IC_{50}) of *ca.* 0.26 μM, which was significantly lower than those of CyO-NEt_2 (IC_{50}, >4 μM) and CyS-NEt_2 (IC_{50}, 2.17 μM), respectively (Table S1†). Although CySe-NEt_2 exhibited a higher dark cytotoxicity (IC_{50}, 5.33 μM) than CyO-NEt_2 (IC_{50}, 12.08 μM) and CyS-NEt_2 (IC_{50}, 8.02 μM), it showed a much higher phototoxicity index (PI, 20.5) over CyO-NEt_2 (PI, <3.0) and CyS-NEt_2 (PI, 3.7). Taken together, among the hetero-atom substituted hemicyanine dyes, the seleniumxanthene-hemicyanine structure outcompeted the other counterparts as efficient PDT/PTT photosensitizers except for the poor photostability and the enhanced dark toxicity, which encouraged us to carry out the following investigation.

Design, characterization and cytotoxicity studies of CySe-$mPEG_{5K}$

To overcome the above-mentioned photostability and dark toxicity issues of CySe-NEt_2, we rationally designed and synthesized a macrotheranostic agent (CySe-$mPEG_{5K}$) through the copper(I)-catalyzed click reaction of CySe-NEt_2 and a PEG chain. The amphiphilic CySe-$mPEG_{5K}$ could directly self-assemble into spherical nanoparticles with a diameter of ~100 nm in aqueous medium, which could be beneficial for tumor targeting *via* the EPR effect (Fig. 3a and b). Besides, the hydrodynamic diameter and TEM results of CySe-$mPEG_{5K}$ in biological aqueous medium DMEM (containing 10% FBS) showed almost no change during 7 days, suggesting the excellent chemical stability of CySe-$mPEG_{5K}$ (Fig. S10†). CySe-$mPEG_{5K}$ displayed an absorption maximum (λ_{max}) of 778 nm and an emission peak located at 816 nm. Notably, CySe-$mPEG_{5K}$ always maintained the monomer absorbance of 778 nm, and no aggregation peak appeared even with the concentration up to 25 μM. In contrast, the increasing concentration of small-molecule counterpart CyX-NEt_2 (X = O, S, Se) caused a blue-shifted absorption shoulder band, indicating the H-aggregation of

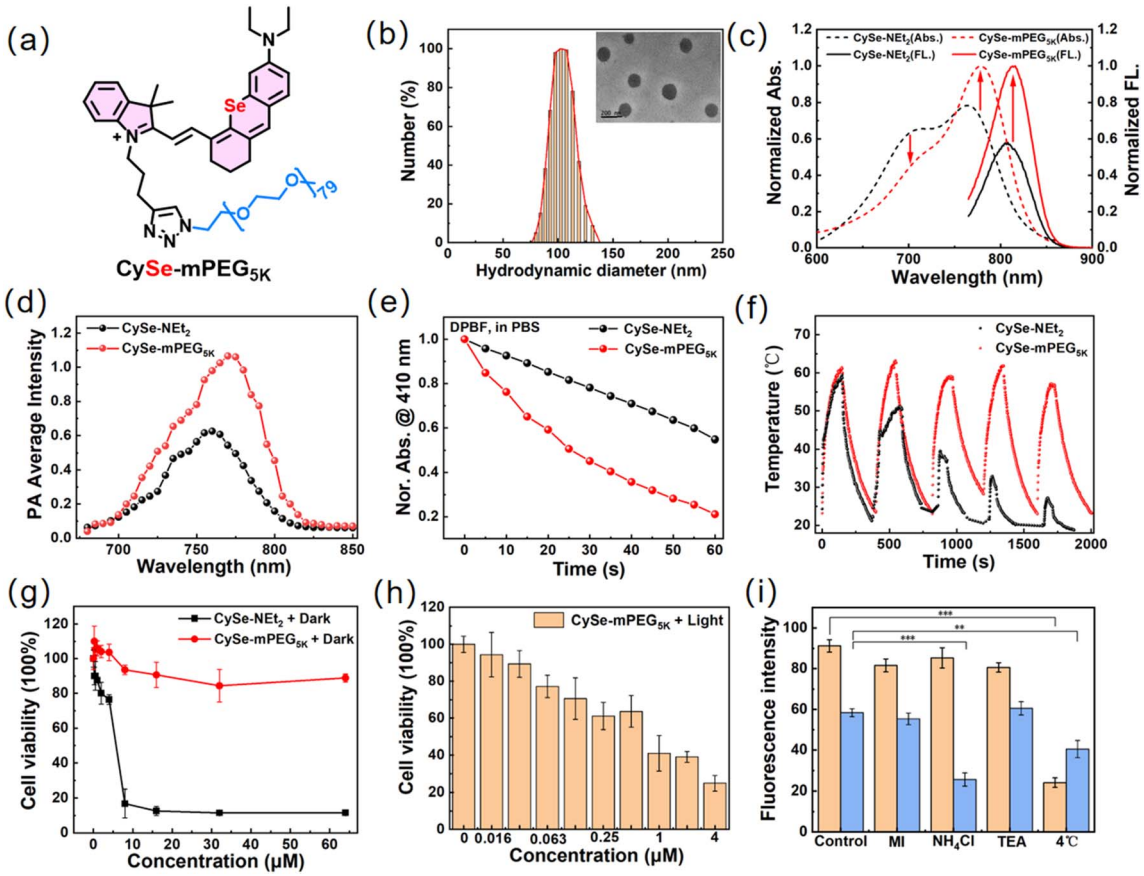

Fig. 3 (a) Chemical structure of CySe-mPEG$_{5K}$. (b) Particle size distribution of CySe-mPEG$_{5K}$ measured in PBS by DLS. Inset: TEM image of nanoparticles, scale bar: 200 nm. Photophysical and photosensitizing properties of CySe-NEt$_2$ and CySe-mPEG$_{5K}$ for (c) normalized absorption and emission spectra in PBS buffer, (d) photoacoustic spectra of CySe-NEt$_2$ and CySe-mPEG$_{5K}$ (100 μM, PBS buffer, pH 7.4), (e) DPBF degradation induced by photosensitizers in PBS under 750 nm light irradiation, 5.0 mW cm^{-2} and (f) photothermal stability study in PBS during five circles of heating–cooling processes (750 nm laser, 500 mW cm^{-2}). (g) Cell viability of 4T1 cells treated with CySe-NEt$_2$ and CySe-mPEG$_{5K}$ at various doses in the dark. (h) Cell viability of 4T1 cells treated with CySe-mPEG$_{5K}$ at various doses under 750 nm light irradiation (90 J cm^{-2}). (i) The fluorescence intensity of 4T1 cells after incubation with CySe-NEt$_2$ and CySe-mPEG$_{5K}$ along with different cell uptake pathway inhibitors. Data are expressed as mean ± SD. *P < 0.05, **P < 0.01, ***P < 0.001.

CyX-NEt$_2$ which leads to fluorescence quenching and photodynamic effect attenuation (Fig. 3c and S11†). As shown in Fig. 3d and S12,† CySe-mPEG$_{5K}$ in PBS displayed a stronger PA signal ranging from 700 to 825 nm than CySe-NEt$_2$, and the dose-dependent linear relationship of PA775 nm intensity offered the possibility for quantitative analysis with photoacoustic imaging signals. Moreover, compared with CySe-NEt$_2$, CySe-mPEG$_{5K}$ maintained the photosensitivity with high $^1O_2$ generation (Φ_Δ = 14.2%) in PBS and inherited high photothermal conversion efficiency (PCE = 40.5%) (Fig. 3e and S13†). More importantly, under 750 nm laser irradiation (500 mW cm^{-2}), the photothermal stability of CySe-mPEG$_{5K}$ was found to be significantly higher than that of CySe-NEt$_2$ (Fig. 3f).[36]

Next, the PDT/PTT performance of CySe-mPEG$_{5K}$ was studied through the MTT assay. CySe-NEt$_2$ exhibited obvious dark cytotoxicity (IC$_{50}$, 5.33 μM) as mentioned above, while negligible cytotoxicity was observed in the CySe-mPEG$_{5K}$ treated group and the viability of 4T1 cells was above 90% even at a high concentration of 64 μM without light irradiation (Fig. 3g). As shown in Fig. 3h, light irradiation (750 nm, 500 mW cm^{-2}) strongly inhibited the proliferation of the CySe-mPEG$_{5K}$ incubated tumor cells (IC$_{50}$ = 0.85 μM), which was inseparable from the light-induced intracellular ROS production (Fig. S14 and S15†).

The cell uptake mechanism was investigated by pretreating the cells with 2-deoxy-D-glucose plus oligomycin (MI, energy metabolism inhibitor), NH_4Cl (transmembrane endocytosis inhibition), or tetraethylammonium chloride (TEA, ion channel blocker) as well as energy blockade at 4 °C for 1 h.[37,38] CLSM images revealed that the cellular uptake of CySe-NEt$_2$ was significantly blocked at 4 °C while that of CySe-mPEG$_{5K}$ was inhibited both at 4 °C and by NH_4Cl treatment. The results indicated that intracellular CySe-mPEG$_{5K}$ accumulation was mainly mediated by transmembrane endocytosis and partly energy-dependent, which differed from the small molecule dye CySe-NEt$_2$ (Fig. 3i and S16†).

Live/dead staining experiments were then performed to visualize the cancer cell-killing ability of CySe-mPEG$_{5K}$ by a live/dead cell costaining viability assay (calcein-AM, green/PI, red)

by CLSM (Fig. S17†). As expected, nearly all the 4T1 cells under the laser-irradiating area were dead (red emission). In contrast, the cellular phototoxicity was barely observed for the cells under the laser at 750 nm without CySe-mPEG$_{5K}$ treatment (green emission), manifesting the low side effect of the applied laser power (0.5 W cm^{-2}). All the above results confirmed that PEG modification endowed CySe-mPEG$_{5K}$ with many advantages, such as suppression of H-aggregation to yield higher NIR fluorescence intensity/PA signal/Φ_{Δ}, excellent photostability, and negligible dark toxicity, suggesting that CySe-mPEG$_{5K}$ could serve as a powerful phototheranostic agent.

Multimodal imaging of 4T1 tumor-xenograft mice

The *in vivo* biodistribution and tumor NIRF and PA imaging capabilities of CySe-mPEG$_{5K}$ were tested in the 4T1 tumor-bearing BALB/c mice model. As shown in Fig. 4a and c, after tail vein injection of 100 μL CySe-mPEG$_{5K}$ (100 μM in the PBS buffer), the NIRF intensity at the tumor site gradually increased

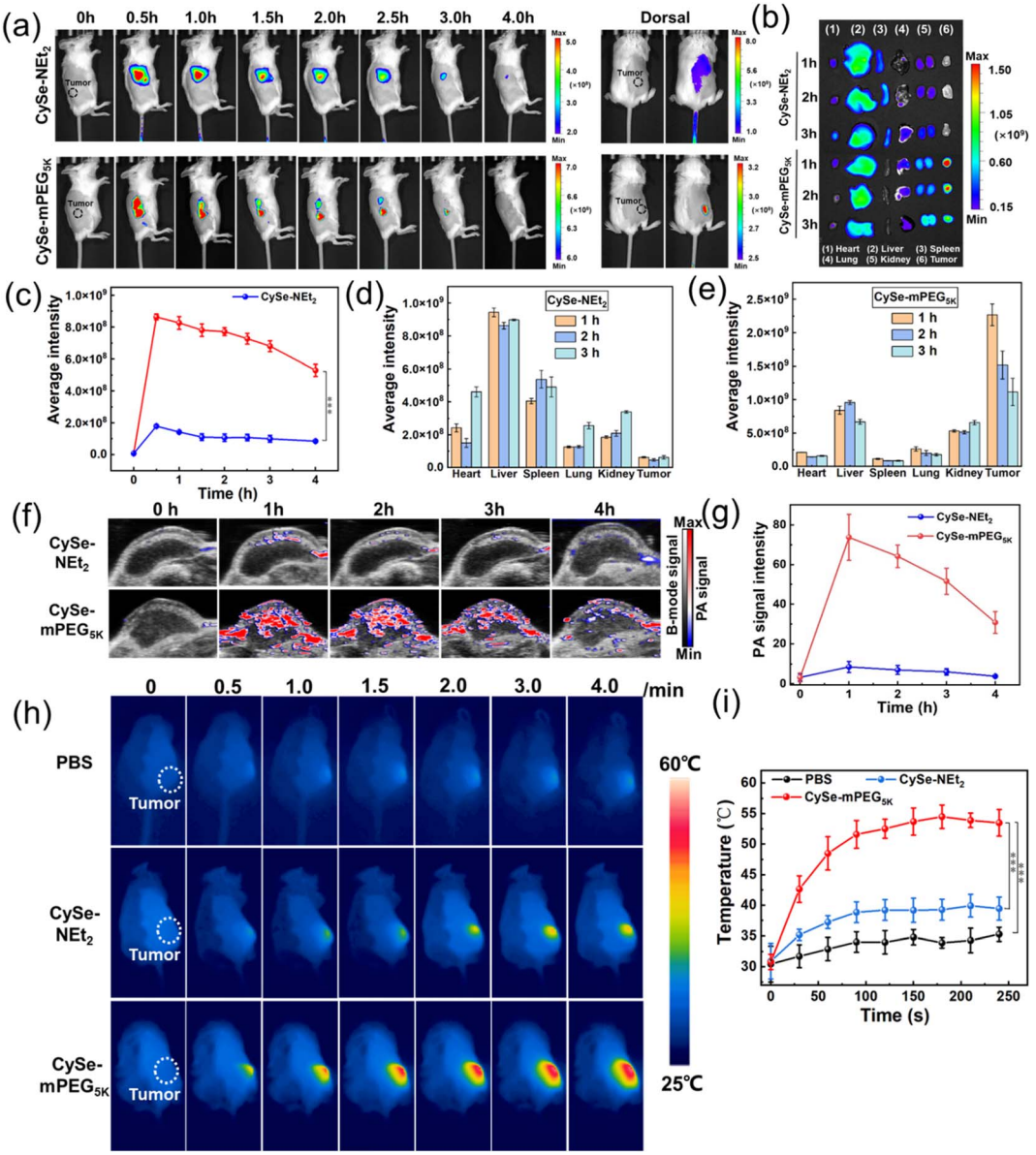

Fig. 4 (a) Fluorescence imaging in the tumor-bearing mice after intravenously injecting with CySe-NEt$_2$ and CySe-mPEG$_{5K}$ (100 μM, 100 μL in the PBS buffer). (b) *In vivo* biodistribution fluorescence images of tumor-bearing mice after intravenous injection of CySe-NEt$_2$ and CySe-mPEG$_{5K}$ for 1 h, 2 h and 3 h. (c) Fluorescence intensity profiles of CySe-NEt$_2$ and CySe-mPEG$_{5K}$ in the tumor sites at different time points. (d and e) Fluorescence intensity profiles of *ex vivo* organs and tumors from the mice in (b) (excitation filter, 760 nm; collected bandpath: 825 ± 20 nm). (f) Representative PA images of tumor regions in living mice at different time points after intravenous injection of CySe-NEt$_2$ and CySe-mPEG$_{5K}$ (200 μM, 100 μL). (g) *In vivo* real-time PA intensity profiles of tumor areas in (f). (h) Thermal images of 4T1 tumor-bearing mice irradiated at 1 h (750 nm, 500 mW cm^{-2}) after i.v. of different solutions. (i) Tumor temperature changing profiles as a function of the imaging time ($n = 3$). Data are expressed as mean ± SD. *P < 0.05, **P < 0.01, ***P < 0.001.

over time and reached maximum values at about 1.0 h post-injection, clearly delineating the shapes of the tumor on the dorsal side. The fluorescence signal began to attenuate after 1.0 h, but was still strong enough to be observed over the next 4 hours. For the small-molecule CySe-NEt_2, its fluorescence signal could not be detected in the tumor region. After mice were sacrificed at 1.0 h, 2.0 h and 3.0 h post-injection, the dissected organs and tumor were collected for *ex vivo* imaging. CySe-$mPEG_{5K}$ exhibited distinct fluorescence in the tumor tissue and could be cleared out through hepatic–renal excretion, while CySe-NEt_2 was mainly accumulated in the liver (Fig. 4b, d and e). PA imaging was further employed to monitor the dynamic accumulation of CySe-$mPEG_{5K}$ in tumors in real-time. As shown in Fig. 4f and g, the PA780 nm signal of CySe-$mPEG_{5K}$ at the tumor region increased greatly and reached the maximum after 1.0 h, which was 8.8-fold higher than that of CySe-NEt_2. The results demonstrated that the macrotheranostic agent CySe-$mPEG_{5K}$ showed fast and selective accumulation in tumor tissue.

Photothermal imaging was conducted at 1.0 h post-injection after intravenous injection of CySe-$mPEG_{5K}$ based on the maximum NIRF and PA signals in the tumor region. The 4T1 tumor-bearing mice were irradiated at 750 nm (0.5 W cm^{-2}) for 4 min and real-time temperatures were recorded using an FLIR thermal mapping camera. As shown in Fig. 4h and i, the temperature of the CySe-$mPEG_{5K}$-treated mice increased remarkably and reached a plateau at 2.0 min, with a maximal tumor temperature of 54.5 °C, which was sufficient to induce tumor cell damage.[39] However, the temperature of CySe-NEt_2 and PBS groups increased slightly, and the final temperature

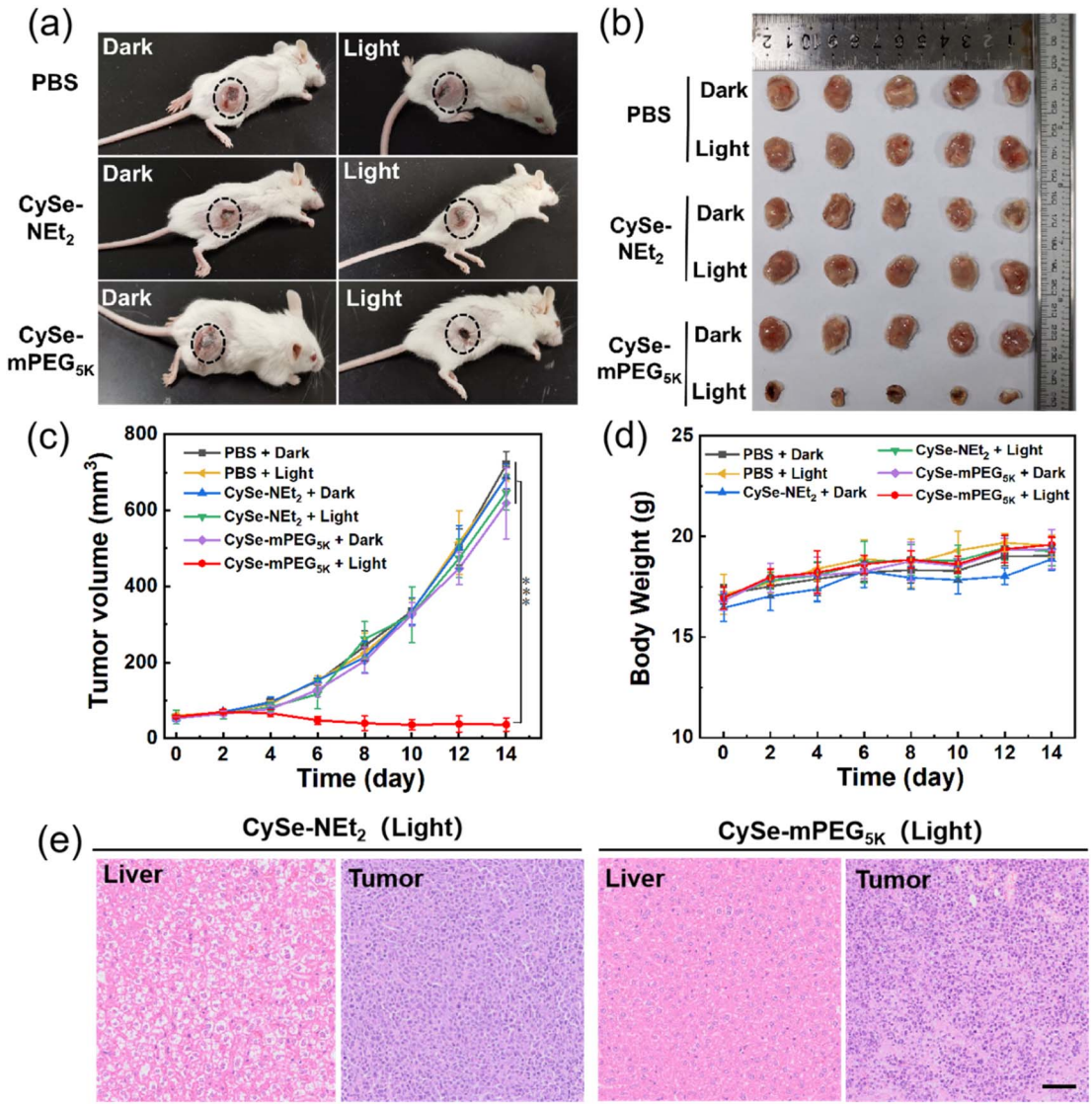

Fig. 5 Images of (a) living mice tumor and (b) dissected tumor after 14 day treatment with different samples. (c) The tumor growth in 4T1 tumor-bearing mice treated with different formulations (200 μM, 100 μL CySe-NEt_2 and CySe-$mPEG_{5K}$ in PBS; in the dark or under 750 nm laser, 500 mW cm^{-2} for 10 min). (d) Body weights of the mice in different groups over time (mean ± SD, $n = 5$). (e) H&E staining of liver and tumor sections in the mice under i.v. injection of CySe-NEt_2 and CySe-$mPEG_{5K}$ with light irradiation at the tumor sites. Scale bar: 100 μm. Data are expressed as mean ± SD. *$P < 0.05$, **$P < 0.01$, ***$P < 0.001$.

was 39.0 and 35.5 °C, respectively. These data proved that the tumor-targeted retention ability of CySe-mPEG$_{5K}$ could be visualized by NIRF, PA and PTT imaging, providing precise guidance for subsequent photo-therapeutic treatment.

In vivo synergistic PDT/PTT therapy evaluation

Finally, the tumor inhibition efficacies of CySe-NEt$_2$ and CySe-mPEG$_{5K}$ under NIR light irradiation *in vivo* were investigated. The CySe-mPEG$_{5K}$-treated 4T1-tumor-bearing mice groups were treated without or with 750 nm laser irradiation at a power density of 500 mW cm^{-2} for 10 min at 1.0 h post-injection. Other two groups of PBS and CySe-NEt$_2$ treated mice (in the dark or under laser), were used as the controls (each group containing five mice). The tumor sizes were measured every 2 days during the 14 days of treatment and relative growth curves were collected. As displayed in Fig. 5a–c, the treatment of CySe-mPEG$_{5K}$ plus light irradiation successfully suppressed the tumor growth because of the higher accumulation and combined PDT/PTT, while negligible therapeutic effect was observed for other groups. Moreover, the body weights of mice changed scarcely during the process of phototherapy (Fig. 5d). Then, the mice were sacrificed after 14 days to obtain hematoxylin and eosin (H&E) staining for histological analysis (Fig. 5e and S18†). As shown in Fig. 5e, the CySe-NEt$_2$-treated group caused noticeable cell necrosis or inflammation lesions in livers resulting from the liver accumulation and dark toxicity of CySe-NEt$_2$, yet no obvious damage to tumor cells was observed. However, the CySe-mPEG$_{5K}$-treatment plus light irradiation induced prominent tumor cell destruction, yet no physiological morphology abnormalities or histopathological lesions were observed for other major organs. These results demonstrated that the tumor-targeted phototherapeutic effect and excellent biocompatibility make CySe-mPEG$_{5K}$ a promising phototheranostic agent for cancer imaging and ablation with minimal toxicity to normal tissues.

Conclusions

In summary, we demonstrated that the Se-substituted xanthene-hemicyanine showed excellent potential as an effective phototheranostic agent. Although there was a 52% loss in fluorescence quantum yield when replacing O atom with Se atom, an over 15-fold increase in $^1O_2$ generation ability and a 53% enhancement of PCE were achieved. Moreover, the much longer excitation/emission wavelength of CySe-NEt$_2$ will lead to better imaging depth. Upon 750 nm irradiation, CySe-NEt$_2$ initiated cell death *via* ROS overproduction and mitochondrial membrane potential loss. Given the inevitable dark cytotoxicity and photobleaching of the Se-hemicyanine dyes, a clickable azide poly(ethylene glycol) (PEG) chain group was introduced into the scaffold to overcome these drawbacks. Modularly derived CySe-mPEG$_{5K}$ demonstrated superior performance such as improved NIR fluorescence/PA signal in PBS, excellent photostability, fast/selective tumor accumulation, and minimum dark toxicity. Moreover, solid tumor growth was significantly suppressed by the effective treatment of the PDT–PTT combination therapy of CySe-mPEG$_{5K}$ under multi-modality imaging guidance. This study provided a powerful platform for the development of effective phototheranostic agents, which is beneficial for precise tumor diagnosis and treatment.

Ethical statement

This study was performed in strict accordance with the guidelines for the care and use of laboratory animals and was approved by the Animal Ethical and Welfare Committee of NJU (Nanjing, China).

Data availability

Data can be available from the corresponding author upon reasonable request.

Author contributions

S. K. Yao and Y. C. Chen designed the study. F. W. Xu and W. Z. Ding synthesized the probes; Z. P. Liu performed the DFT calculations; S. K. Yao performed the cellular experiments, MTT experiments, the *in vivo* experiments; S. K. Yao and W. Z. Ding co-wrote the manuscript. W. J. He, Z. J. Guo and Y. C. Chen conceived the project and revised the manuscript. All authors discussed the results and commented on the paper. All authors have given approval to the final version of the manuscript.

Conflicts of interest

The authors declare no competing interests.

Acknowledgements

This work was financially supported by the Natural Science Foundation of China (22122701, 21731004, 21907050, 92153303, 91953201, 21977044), the Natural Science Foundation of Jiangsu Province (BK20202004), the Excellent Research Program of Nanjing University (ZYJH004) and the Open Research Fund of the National Center for Protein Sciences at Peking University in Beijing (KF-202201).

Notes and references

1 X. Wei, C. Zhang, S. S. He, J. G. Huang, J. S. Huang, S. S. Liew, Z. L. Zeng and K. Y. Pu, *Angew. Chem., Int. Ed.*, 2022, **61**, e202202966.
2 G. X. Feng, G. Q. Zhang and D. Ding, *Chem. Soc. Rev.*, 2020, **49**, 8179–8234.
3 J. Xing, Q. Y. Gong, O. U. Akakuru, C. Liu, R. F. Zou and A. Wu, *Nanoscale*, 2020, **12**, 24311–24330.
4 S. M. Usama, S. Thavornpradit and K. Burgess, *ACS Appl. Bio Mater.*, 2018, **1**, 1195–1205.
5 H. Y. Wang, J. J. Chang, M. W. Shi, W. Pan, N. Li and B. Tang, *Angew. Chem., Int. Ed.*, 2019, **58**, 1057–1061.

6 L. X. Sun, J. Wang, B. C. Yang, X. X. Wang, G. X. Yang, X. Q. Wang, Y. Y. Jiang, T. Y. Wang and J. Z. Jiang, *RSC Adv.*, 2021, **11**, 10061–10074.
7 V. N. Nguyen, S. Qi, S. Kim, N. Kwon, G. Kim, Y. Yim, S. Park and J. Yoon, *J. Am. Chem. Soc.*, 2019, **141**(41), 16243–16248.
8 H. Ma, Y. Lu, Z. B. Huang, S. Long, J. F. Cao, Z. Zhang, X. Zhou, C. Shi, W. Sun, J. J. Du, J. L. Fan and X. J. Peng, *J. Am. Chem. Soc.*, 2022, **144**, 3477–3486.
9 M. H. Lan, S. J. Zhao, W. M. Liu, C. S. Lee, W. J. Zhang and P. F. Wang, *Adv. Healthcare Mater.*, 2019, **8**, 1900132.
10 X. Z. Zhao, S. Long, M. L. Li, J. F. Cao, Y. C. Li, L. Y. Guo, W. Sun, J. J. Du, J. L. Fan and X. J. Peng, *J. Am. Chem. Soc.*, 2020, **142**, 1510–1517.
11 H. S. Jung, P. Verwilst, A. Sharma, J. Shin, J. L. Sessler and J. S. Kim, *Chem. Soc. Rev.*, 2018, **47**, 2280–2297.
12 Y. Huang, N. He, Y. Q. Wang, D. Z. Shen, Q. Kang, R. F. Zhao and L. X. Chen, *J. Mater. Chem. B*, 2019, **7**, 1149–1159.
13 Y. C. Liu, C. Y. Xu, L. L. Teng, H. W. Liu, T. B. Ren, S. Xu, X. F. Lou, H. W. Guo, L. Yuan and X. B. Zhang, *Chem. Commun.*, 2020, **56**, 1956–1959.
14 J. J. Zhang, L. L. Ning, J. G. Huang, C. Zhang and K. Y. Pu, *Chem. Sci.*, 2020, **11**, 618–630.
15 J. H. Zou, P. Wang, Y. Wang, G. Y. Liu, Y. W. Zhang, Q. Zhang, J. J. Shao, W. L. Si, W. Huang and X. C. Dong, *Chem. Sci.*, 2019, **10**, 268–276.
16 Y. J. Liu, P. Bhattarai, Z. F. Dai and X. Y. Chen, *Chem. Soc. Rev.*, 2019, **48**, 2053–2108.
17 Z. X. Zhao, C. B. Swartchick and J. Chan, *Chem. Soc. Rev.*, 2022, **51**, 829–868.
18 Q. Q. Miao and K. Y. Pu, *Bioconjugate Chem.*, 2016, **27**, 2808–2823.
19 L. Yuan, W. L. Lin, S. Zhao, W. S. Gao, B. Chen, L. W. He and S. Zhu, *J. Am. Chem. Soc.*, 2012, **134**, 13510–13523.
20 L. Yuan, W. Y. Lin, Y. T. Yang and H. Chen, *J. Am. Chem. Soc.*, 2012, **134**, 1200–1211.
21 S. H. Gardner, C. J. Brady, C. Keeton, A. K. Yadav, S. C. Mallojjala, M. Y. Lucero, S. Su, Z. Yu, J. S. Hirschi, L. M. Mirica and J. Chan, *Angew. Chem., Int. Ed.*, 2021, **60**, 18860–18866.
22 H. D. Li, H. Kim, F. Xu, J. J. Han, Q. C. Yao, J. Y. Wang, K. Y. Pu, X. J. Peng and J. Yoon, *Chem. Soc. Rev.*, 2022, **51**, 1795–1835.
23 P. H. Cheng and K. Y. Pu, *Nat. Rev. Mater.*, 2021, **6**, 1095–1113.
24 Y. Zhang, S. S. He, C. Xu, Y. Jiang, Q. Q. Miao and K. Y. Pu, *Angew. Chem., Int. Ed.*, 2022, **61**, e202203184.
25 Z. L. Zeng, S. S. Liew, X. Wei and K. Y. Pu, *Angew. Chem., Int. Ed.*, 2021, **60**, 26454–26475.
26 M. Lucero and J. Jefferson Chan, *Nat. Chem.*, 2021, **13**, 1248–1256.
27 P. H. Cheng, Q. Q. Miao, J. C. Li, J. G. Huang, C. Xie and K. Y. Pu, *J. Am. Chem. Soc.*, 2019, **141**, 10581–10584.
28 H. W. Liu, X. X. Hu, K. Li, Y. C. Liu, Q. M. Rong, L. M. Zhu, L. Yuan, F. L. Qu, X. B. Zhang and W. H. Tan, *Chem. Sci.*, 2017, **8**, 7689–7695.
29 T. M. Ebaston, F. Nakonechny, E. Talalai, G. Gellerman and L. Patsenker, *Dyes Pigm.*, 2021, **184**, 108854.
30 M. Santra, M. Owens, G. Birch and M. Bradley, *ACS Appl. Bio Mater.*, 2021, **4**, 8503–8508.
31 F. Xu, H. D. Li, Q. C. Yao, H. Y. Ge, J. L. Fan, W. Sun, J. Y. Wang and X. J. Peng, *Chem. Sci.*, 2019, **10**, 10586–10594.
32 X. Xia, R. Wang, Y. Q. Hu, Q. C. Yao, S. Long, W. Sun, J. L. Fan and X. J. Peng, *Sci. China: Chem.*, 2022, **65**, 821–828.
33 S. P. Zhang, H. Chen, L. P. Wang, X. Qin, B. P. Jiang, S. C. Ji, X. C. Shen and H. Liang, *Angew. Chem., Int. Ed.*, 2022, **134**, e202107076.
34 Y. T. Zhang, C. X. Yan, Q. Q. Zheng, Q. Jia, Z. L. Wang, P. Shi and Z. Q. Guo, *Angew. Chem., Int. Ed.*, 2021, **60**, 9553–9561.
35 W. Sun, S. G. Guo, C. Hu, J. L. Fan and X. J. Peng, *Chem. Rev.*, 2016, **116**, 7768–7817.
36 X. Zhen, J. J. Zhang, J. G. Huang, C. Xie, Q. Q. Miao and K. Y. Pu, *Angew. Chem., Int. Ed.*, 2018, **57**, 7804–7808.
37 X. J. Zhao, H. J. Zhao, S. Wang, Z. W. Fan, Y. Ma, Y. M. Yin, W. Wang, R. M. Xi and M. Meng, *J. Am. Chem. Soc.*, 2021, **143**, 20828–20836.
38 K. W. Wang, X. Xiao, M. L. Jiang, J. S. Li, J. L. Zhou and Y. Y. Yuan, *Small*, 2021, **17**, 2102610.
39 Z. Y. Jiang, C. L. Zhang, X. Q. Wang, M. Yan, Z. X. Ling, Y. C. Chen and Z. P. Liu, *Angew. Chem., Int. Ed.*, 2021, **60**, 22376–22384.